Biomedical Optics EXPRESS

Multimodal optical imaging system for *in vivo* investigation of cerebral oxygen delivery and energy metabolism

Mohammad A. Yaseen,[1,*] Vivek J. Srinivasan,[1,2] Iwona Gorczynska,[3,4] James G. Fujimoto,[3] David A. Boas,[1] and Sava Sakadžić[1]

[1]*Department of Radiology, MGH/MIT/HMS Athinuola A. Martinos Center for Biomedical Imaging, Massachusetts General Hospital, Harvard Medical School, Charlestown, Massachusetts, USA*
[2]*Current Affiliation: Department of Biomedical Engineering, University of California, Davis, Davis, California, USA*
[3]*Department of Electrical Engineering and Computer Science and Research Laboratory of Electronics, Massachusetts Institute of Technology, Cambridge, Massachusetts, USA*
[4]*Current Affiliation: Department of Biophysics and Medical Physics, Institute of Physics, Nicolaus Copernicus University, Torun, Poland*
**mayaseen@nmr.mgh.harvard.edu*

Abstract: Improving our understanding of brain function requires novel tools to observe multiple physiological parameters with high resolution *in vivo*. We have developed a multimodal imaging system for investigating multiple facets of cerebral blood flow and metabolism in small animals. The system was custom designed and features multiple optical imaging capabilities, including 2-photon and confocal lifetime microscopy, optical coherence tomography, laser speckle imaging, and optical intrinsic signal imaging. Here, we provide details of the system's design and present *in vivo* observations of multiple metrics of cerebral oxygen delivery and energy metabolism, including oxygen partial pressure, microvascular blood flow, and NADH autofluorescence.

OCIS codes: (170.0110) Imaging systems; (110.4190) Multiple imaging; (180.4315) Nonlinear microscopy; (170.4500) Optical coherence tomography.

References and links

1. C. S. Roy and C. S. Sherrington, "On the regulation of the blood-supply of the brain," J. Physiol. **11**(1-2), 158 (1890).
2. M. E. Raichle, "A brief history of human brain mapping," Trends Neurosci. **32**(2), 118–126 (2009).
3. K. Bartlett, M. Saka, and M. Jones, "Polarographic Electrode Measures of Cerebral Tissue Oxygenation: Implications for Functional Brain Imaging," Sensors (Basel Switzerland) **8**(12), 7649–7670 (2008).
4. J. J. Riera, A. Schousboe, H. S. Waagepetersen, C. Howarth, and F. Hyder, "The micro-architecture of the cerebral cortex: functional neuroimaging models and metabolism," Neuroimage **40**(4), 1436–1459 (2008).
5. A. Devor, S. Sakadžić, V. J. Srinivasan, M. A. Yaseen, K. Nizar, P. A. Saisan, P. Tian, A. M. Dale, S. A. Vinogradov, M. A. Franceschini, and D. A. Boas, "Frontiers in optical imaging of cerebral blood flow and metabolism," J. Cereb. Blood Flow Metab. **32**(7), 1259–1276 (2012).
6. A. Kumar and T. C. Foster, "Neurophysiology of old neurons and synapses," in *Brain Aging: Models, Methods, and Mechanisms*, D. R. Riddle, ed. (Boca Raton, FL: CRC Press, 2007).
7. M. T. Lin and M. F. Beal, "Mitochondrial dysfunction and oxidative stress in neurodegenerative diseases," Nature **443**(7113), 787–795 (2006).
8. D. C. Wallace, "A mitochondrial paradigm of metabolic and degenerative diseases, aging, and cancer: a dawn for evolutionary medicine," Annu. Rev. Genet. **39**(1), 359–407 (2005).
9. C. Catana, A. Drzezga, W.-D. Heiss, and B. R. Rosen, "PET/MRI for neurologic applications," J. Nucl. Med. **53**(12), 1916–1925 (2012).
10. F. Scholkmann, S. Kleiser, A. J. Metz, R. Zimmermann, J. Mata Pavia, U. Wolf, and M. Wolf, "A review on continuous wave functional near-infrared spectroscopy and imaging instrumentation and methodology," Neuroimage **85**(Pt 1), 6–27 (2014).
11. K. A. Kasischke, H. D. Vishwasrao, P. J. Fisher, W. R. Zipfel, and W. W. Webb, "Neural activity triggers neuronal oxidative metabolism followed by astrocytic glycolysis," Science **305**(5680), 99–103 (2004).

#248448 Received 25 Aug 2015; revised 9 Nov 2015; accepted 14 Nov 2015; published 20 Nov 2015

12. V. J. Srinivasan, S. Sakadzić, I. Gorczynska, S. Ruvinskaya, W. Wu, J. G. Fujimoto, and D. A. Boas, "Depth-resolved microscopy of cortical hemodynamics with optical coherence tomography," Opt. Lett. **34**(20), 3086–3088 (2009).
13. S. Sakadžić, E. Roussakis, M. A. Yaseen, E. T. Mandeville, A. Devor, E. H. Lo, S. A. Vinogradov, and D. A. Boas, "Imaging of oxygen partial pressure in cerebral vasculature and tissue using a two-photon-enhanced phosphorescent nanoprobe," Nat. Methods **7**, 755–759 (2010).
14. M. A. Yaseen, V. J. Srinivasan, S. Sakadžić, H. Radhakrishnan, I. Gorczynska, W. Wu, J. G. Fujimoto, and D. A. Boas, "Microvascular oxygen tension and flow measurements in rodent cerebral cortex during baseline conditions and functional activation," J. Cereb. Blood Flow Metab. **31**(4), 1051–1063 (2011).
15. S. Sakadžić, E. T. Mandeville, L. Gagnon, J. J. Musacchia, M. A. Yaseen, M. A. Yucel, J. Lefebvre, F. Lesage, A. M. Dale, K. Eikermann-Haerter, C. Ayata, V. J. Srinivasan, E. H. Lo, A. Devor, and D. A. Boas, "Large arteriolar component of oxygen delivery implies a safe margin of oxygen supply to cerebral tissue," Nat. Commun. **5**, 5734 (2014).
16. M. A. Yaseen, S. Sakadžić, W. Wu, W. Becker, K. A. Kasischke, and D. A. Boas, "In vivo imaging of cerebral energy metabolism with two-photon fluorescence lifetime microscopy of NADH," Biomed. Opt. Express **4**(2), 307–321 (2013).
17. M. A. Yaseen, V. J. Srinivasan, S. Sakadzić, W. Wu, S. Ruvinskaya, S. A. Vinogradov, and D. A. Boas, "Optical monitoring of oxygen tension in cortical microvessels with confocal microscopy," Opt. Express **17**(25), 22341–22350 (2009).
18. V. J. Srinivasan, S. Sakadzić, I. Gorczynska, S. Ruvinskaya, W. Wu, J. G. Fujimoto, and D. A. Boas, "Quantitative cerebral blood flow with Optical Coherence Tomography," Opt. Express **18**(3), 2477–2494 (2010).
19. D. A. Boas and A. K. Dunn, "Laser speckle contrast imaging in biomedical optics," J. Biomed. Opt. **15**(1), 011109 (2010).
20. A. K. Dunn, A. Devor, H. Bolay, M. L. Andermann, M. A. Moskowitz, A. M. Dale, and D. A. Boas, "Simultaneous imaging of total cerebral hemoglobin concentration, oxygenation, and blood flow during functional activation," Opt. Lett. **28**(1), 28–30 (2003).
21. M. B. Bouchard, B. R. Chen, S. A. Burgess, and E. M. C. Hillman, "Ultra-fast multispectral optical imaging of cortical oxygenation, blood flow, and intracellular calcium dynamics," Opt. Express **17**(18), 15670–15678 (2009).
22. A. K. Dunn, A. Devor, A. M. Dale, and D. A. Boas, "Spatial extent of oxygen metabolism and hemodynamic changes during functional activation of the rat somatosensory cortex," Neuroimage **27**(2), 279–290 (2005).
23. A. Y. Shih, J. D. Driscoll, P. J. Drew, N. Nishimura, C. B. Schaffer, and D. Kleinfeld, "Two-photon microscopy as a tool to study blood flow and neurovascular coupling in the rodent brain," J. Cereb. Blood Flow Metab. **32**(7), 1277–1309 (2012).
24. I. Dunphy, S. A. Vinogradov, and D. F. Wilson, "Oxyphor R2 and G2: phosphors for measuring oxygen by oxygen-dependent quenching of phosphorescence," Anal. Biochem. **310**(2), 191–198 (2002).
25. S. Sakadzić, S. Yuan, E. Dilekoz, S. Ruvinskaya, S. A. Vinogradov, C. Ayata, and D. A. Boas, "Simultaneous imaging of cerebral partial pressure of oxygen and blood flow during functional activation and cortical spreading depression," Appl. Opt. **48**(10), D169–D177 (2009).
26. T. Kim, K. S. Hendrich, K. Masamoto, and S.-G. Kim, "Arterial versus total blood volume changes during neural activity-induced cerebral blood flow change: implication for BOLD fMRI," J. Cereb. Blood Flow Metab. **27**(6), 1235–1247 (2007).
27. O. S. Finikova, A. Y. Lebedev, A. Aprelev, T. Troxler, F. Gao, C. Garnacho, S. Muro, R. M. Hochstrasser, and S. A. Vinogradov, "Oxygen microscopy by two-photon-excited phosphorescence," Chem. Phys. Chem. **9**, 1673–1679 (2008).
28. J. Lecoq, A. Parpaleix, E. Roussakis, M. Ducros, Y. Goulam Houssen, S. A. Vinogradov, and S. Charpak, "Simultaneous two-photon imaging of oxygen and blood flow in deep cerebral vessels," Nat. Med. **17**(7), 893–898 (2011).
29. Q. Fang, S. Sakadzić, L. Ruvinskaya, A. Devor, A. M. Dale, and D. A. Boas, "Oxygen advection and diffusion in a three- dimensional vascular anatomical network," Opt. Express **16**(22), 17530–17541 (2008).
30. P. S. Tsai, J. P. Kaufhold, P. Blinder, B. Friedman, P. J. Drew, H. J. Karten, P. D. Lyden, and D. Kleinfeld, "Correlations of neuronal and microvascular densities in murine cortex revealed by direct counting and colocalization of nuclei and vessels," J. Neurosci. **29**(46), 14553–14570 (2009).
31. B. V. Zlokovic, "Neurovascular pathways to neurodegeneration in Alzheimer's disease and other disorders," Nat. Rev. Neurosci. **12**(12), 723–738 (2011).
32 R. B. Buxton, "Interpreting oxygenation-based neuroimaging signals: the importance and the challenge of understanding brain oxygen metabolism," Front. Neuroenergetics **2**, 8 (2010).
33. A. Devor, S. Sakadžić, P. A. Saisan, M. A. Yaseen, E. Roussakis, V. J. Srinivasan, S. A. Vinogradov, B. R. Rosen, R. B. Buxton, A. M. Dale, and D. A. Boas, "Overshoot' of O_2 is required to maintain baseline tissue oxygenation at locations distal to blood vessels," J. Neurosci. **31**(38), 13676–13681 (2011).
34. H. D. Vishwasrao, A. A. Heikal, K. A. Kasischke, and W. W. Webb, "Conformational Dependence of Intracellular NADH on Metabolic State Revealed by Associated Fluorescence Anisotropy," J. Biol. Chem. **280**(26), 25119–25126 (2005).

#248448 Received 25 Aug 2015; revised 9 Nov 2015; accepted 14 Nov 2015; published 20 Nov 2015

35. M. C. Skala, K. M. Riching, A. Gendron-Fitzpatrick, J. Eickhoff, K. W. Eliceiri, J. G. White, and N. Ramanujam, "In vivo multiphoton microscopy of NADH and FAD redox states, fluorescence lifetimes, and cellular morphology in precancerous epithelia," Proc. Natl. Acad. Sci. U.S.A. **104**(49), 19494–19499 (2007).
36. W. Becker, *Advanced Time-Correlated Single Photon Counting Techniques* (Berlin, Heidelberg, New York: Springer, 2005).
37. Q. Yu and A. A. Heikal, "Two-photon autofluorescence dynamics imaging reveals sensitivity of intracellular NADH concentration and conformation to cell physiology at the single-cell level," J. Photochem. Photobiol. B **95**(1), 46–57 (2009).
38. T. H. Chia, A. Williamson, D. D. Spencer, and M. J. Levene, "Multiphoton fluorescence lifetime imaging of intrinsic fluorescence in human and rat brain tissue reveals spatially distinct NADH binding," Opt. Express **16**(6), 4237–4249 (2008).
39. E. Beaurepaire, L. Moreaux, F. Amblard, and J. Mertz, "Combined scanning optical coherence and two-photon-excited fluorescence microscopy," Opt. Lett. **24**(14), 969–971 (1999).
40. S. Tang, Y. Zhou, K. K. H. Chan, and T. Lai, "Multiscale multimodal imaging with multiphoton microscopy and optical coherence tomography," Opt. Lett. **36**(24), 4800–4802 (2011).
41. S. P. Chong, T. Lai, Y. Zhou, and S. Tang, "Tri-modal microscopy with multiphoton and optical coherence microscopy/tomography for multi-scale and multi-contrast imaging," Biomed. Opt. Express **4**(9), 1584–1594 (2013).
42. B. Jeong, B. Lee, M. S. Jang, H. Nam, S. J. Yoon, T. Wang, J. Doh, B.-G. Yang, M. H. Jang, and K. H. Kim, "Combined two-photon microscopy and optical coherence tomography using individually optimized sources," Opt. Express **19**(14), 13089–13096 (2011).
43. B. Kim, T. J. Wang, Q. Li, J. Nam, S. Hwang, E. Chung, S. Kim, and K. H. Kim, "Combined two-photon microscopy and angiographic optical coherence tomography," J. Biomed. Opt. **18**(8), 080502 (2013).

1. Introduction

Brain function requires a tightly-regulated relationship between neuronal signaling activity, energy metabolism, and cerebral blood flow (CBF). While awareness of the relationship between cerebral blood flow and energy metabolism has existed for over a century, precise details of its underlying mechanisms and its dynamic, stimulus-induced local uncoupling, referred to as the hemodynamic response, remain poorly understood [1–5]. Additionally, the onset, progression, or advanced stages of numerous pathological conditions, including stroke, cancer, and neurodegenerative conditions such as Alzheimer's disease reportedly involve notable compromises in signaling and energy metabolism and adverse alterations in cerebral blood flow [6–8]. Obtaining a detailed, mechanistic understanding of neuronal and glial activity and metabolism and their influence on cerebral blood flow is crucial for understanding brain function and its pathological alterations. Although profound insights into brain architecture and function have been revealed from both macroscopic neuroimaging techniques such as positron emission tomography and/or magnetic resonance imaging [9], and near infrared spectroscopy [10], as well as microscopic studies of cell cultures and brain slices [11], advancing our knowledge ideally requires tools to perform high-resolution assessment of multiple physiological parameters, preferably simultaneously, within the living brain *in vivo*, in which the complex morphology and functional relationships between neurons, glial cells, and blood vessels remain preserved. We have developed a multimodal optical imaging system for investigating cerebral metabolism and hemodynamics with high spatial and temporal resolution *in vivo*. The system enables minimally-invasive characterization of multiple parameters of cerebral energetics in a living animal with microscopic resolution, including absolute blood flow, intravascular and tissue oxygen partial pressure (pO_2), nicotinamide adenide dinucleotide (NADH) autofluorescence, and calcium signaling, and it is useful for detailed investigations of the complex interplay between cerebral microvasculature and various cell types in both healthy and diseased brains [12–14]. Here, we present technical details of the system's design and show observations collected with the system of various cerebral metabolic parameters from living rats and mice. The system features a variety of optically-based measurement capabilities, including 2-photon (TPM) and confocal microscopy, optical coherence tomography (OCT), laser speckle contrast imaging (LSCI), and optical intrinsic signal imaging. Several of the presented modalities have been described separately in prior publications [13–16]. Some of the imaging methods offer

#248448 Received 25 Aug 2015; revised 9 Nov 2015; accepted 14 Nov 2015; published 20 Nov 2015

redundant capabilities for measuring markers of cerebral metabolism. Examples include the ability to measure oxygen partial pressure using either TPM or confocal microscopy, and OCT and LSCI both enable monitoring of cerebral blood flow. In practice, each technique offers distinct benefits and limitations, including contrast mechanism, temporal and spatial resolution, optical penetration depths, field of view, complexity, expense, and ease of coupling with other measurement methods. Confocal microscopy and LSCI provide the ability to measure oxygenation and blood flow over larger fields of view with more economical hardware and resources. Conversely, TPM and OCT enable more comprehensive, high resolution studies with absolute quantitation ability at deeper regions in the cerebral cortex but require utilizing more costly instrumentation, contrast agents, and computational resources. Overall, integrating these modalities into a single imaging platform offers unique opportunities to nondestructively, often simultaneously, measure multiple metrics of cerebral blood flow and metabolism at different temporal and spatial scales, enabling more comprehensive, multifaceted investigations of cerebral function in healthy and diseased states.

2. System description and methods

2.1 Custom imaging system specifications

Figure 1 illustrates the principal features of our customized multimodal microscope, specifically developed for *in vivo* cortical imaging of small animals such as rats and mice. The upright microscope was designed to simultaneously monitor multiple metabolic parameters such as microvascular blood flow and cerebral oxygenation. Table 1 details the optical modalities incorporated into the microscope and lists their primary applications for characterizing in vivo cerebral metabolism. The listed spatial and temporal resolutions as well as penetration depths are characteristic for in vivo cerebral metabolism investigations conducted using the presented multimodal microscope. Of these methods, TPM and LSCI can currently be performed simultaneously, as can confocal and OCT [14]. A platform to secure the animal subject is situated atop programmable xy- stages (Physik Instrument) directly beneath an objective lens affixed on a programmable z-stage. TPM or confocal excitation are achieved by guiding a pulsed, tunable Ti:Sapphire laser beam (λ: 730-980 nm, MaiTai, Spectra Physics) or a continuous-wave diode laser beam (λ = 532 nm, B & W Tek), respectively, through one of the system's 2 scanning paths coupled together by a custom dichroic mirror (λ_{cutoff} = 750 nm; Chroma Technologies, Bellows Falls, VT). Laser excitation intensity is rapidly gated using an electro-optic modulator (ConOptics, Model 350-160BK, Danbury CT). A pair of galvanometer-based scanner mirrors (6215HB, Cambridge Technology, Inc) directs the excitation light through a scan lens (AC254-030-B, F = 30 mm, Thorlabs Inc), tube lens (F = 180 mm) inside a microscope trinocular (U-TR30IR, Olympus, not shown), and a microscope objective onto the sample. In general for our experiments, a 4x objective (Olympus XLFluor x4, 0.28 NA) is utilized for measurements over a ~2.5 – 3 mm field of view, while a 20x objective (Olympus XLumPlan Fluor, 20X, 1.00 NA, 2 mm working distance) is used for higher resolution measurements over fields of view ranging from 50 - ~700 μm. Typical excitation powers do not exceed few mW for both confocal and TPM imaging.

#248448 Received 25 Aug 2015; revised 9 Nov 2015; accepted 14 Nov 2015; published 20 Nov 2015

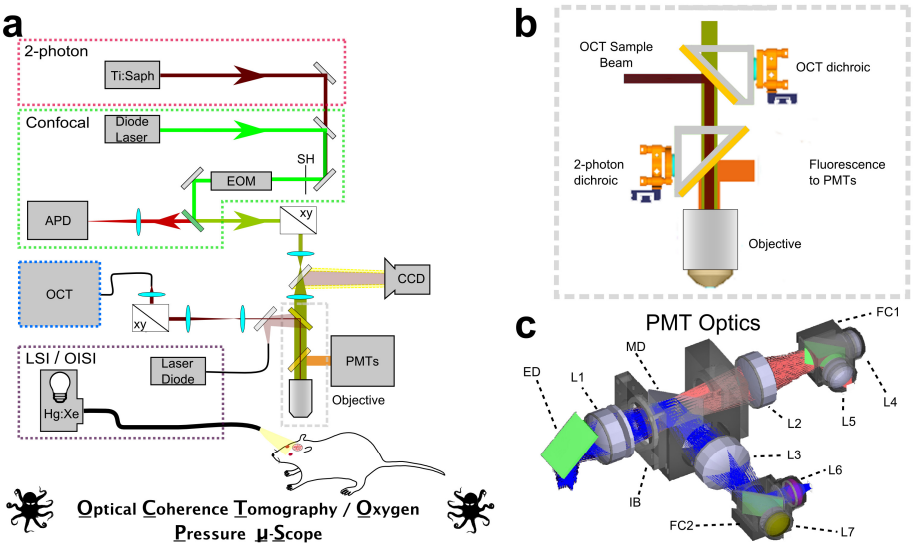

Fig. 1. (**a**). Schematic featuring primary components of the custom multimodal optical microscope. EOM- electro-optic modulator, SH- shutter, APD- avalanche photodiode, xy-galvanometer scanners, Hg:Xe- arc lamp. (**b**) Magnified region of schematic illustrating how the TPM/confocal scanning beam path and OCT beam path are coupled together and how emitted fluorescence is separated. OCT and TPM/confocal modules were designed with separate scanning arms and their probing optical beams were coupled into the same microscope objective by a movable dichroic mirror. (**c**) Detailed model of detector array for TPM fluorescence. Some specifications ED: Epi dichroic after objective (FF735-Di01-25x36, Semrock Inc), IB: Infrared blocker (FF01-750/SP-50, Semrock Inc), MD: main dichroic mirror (t560lpxr-35x52, Chroma Technology Corp), FC1: Filter Cube 1 (dichroic mirror: t640lpxr; channel 1 emission filter: hq680-60m-TPM; channel 2 emission filter: et595/50m-TPM, Chroma Technology Corp), FC2: Filter Cube 2 (dichroic mirror: FF495-Di02-25x36; channel 3 emission filter: FF01-525/50-25; channel 4 emission filter: FF01-460/60-25, Semrock Inc), L1-L3: Lenses 1-3: 50 mm diameter; FL = 81 mm (026-1450, OptoSigma Corporation), L4-L7: Lenses 4-7: 25.4 mm diameter, FL = 19 mm (KBX043, Newport).

In the case of TPM imaging, large-etendue collection optics (15 mm^2 sr) were designed to maximize imaging depth in highly scattering rodent brain tissue (Fig. 1(c)). Emitted fluorescence or phosphorescence is collected by the objective, directed to detectors by an epi-dichroic mirror positioned immediately above the objective, and initially filtered by an infrared blocker. The emission light is guided to an array of photomultiplier tubes using 2-inch diameter lenses and IR blockers, followed by 1-inch emission filters and focusing lenses. The TPM detector consists of four channels covering a wide range of emission wavelength bands from different fluorophores (Channel 1: 680 ± 30 nm, Channel 2: 595 ± 25 nm, Channel 3: 525 ± 25 nm, and Channel 4: 460 ± 30 nm).

For confocal imaging, emitted light is first de-scanned by propagating backward through the telescope and galvo-mirrors. The emission is subsequently spectrally filtered by another dichroic and emission filter and focused onto an avalanche photodiode (APD, SPCM-AQRH-10, Perkin Elmer, Waltham, MA). In place of a pinhole, the active area of the APD (180 μm diameter) operates as the spatial filter of the detected signal. The confocal APD and channels 1 and 4 of the PMT array use photon counting circuitry, enabling lifetime imaging of fluorescence and phosphorescence. Phosphorescence lifetime and fluorescence intensity imaging are performed using NI PCIe-6537, NI PCI 6713, and NI PCI6115 (National Instruments, Austin TX) data acquisition control boards and custom-designed control software in LabView and C [12, 17]. Fluorescence lifetime imaging microscopy (FLIM) is performed by directing the PMT signals to commercial time-correlated single photon

#248448 Received 25 Aug 2015; revised 9 Nov 2015; accepted 14 Nov 2015; published 20 Nov 2015

Table 1. Applications and characteristics of incorporated imaging modalities [5]

Imaging Modality	Observable Morphologic and Metabolic Parameters	Contrast Mechanism	Spatial Resolution	Penetration Depth	Temporal Resolution
Confocal Microscopy	Absolute pO_2, pial vessel angiography	Phosphorescence and fluorescence lifetime and intensity	~1-5 μm	~200 μm	~10ms – 10 s
LSCI	relative CBF	Optical scattering	~20–200 μm	~200 μm	~10 – 100 ms
OCT	Absolute CBF, angiography, RBC speed and flux	Optical scattering	~3-15 μm	~1000 μm	~10 ms – 200s
OISI	relative changes in HbO, HbR, HbT, and (in combination with LSCI) relative CMRO2	Optical absorbance and scattering	~20–200 μm	~200 μm	~10 – 100 ms
TPM	Absolute pO_2, NADH and calcium dynamics and relative concentration, cell morphology, angiography, absolute RBC speed/flux	Phosphorescence and fluorescence lifetime and intensity, second harmonic generation	~1-5 μm	~700 μm	~10 ms – 200s

counting (TCSPC) electronics (SPC-150, and DCC-100, Becker & Hickl GmbH) [16]. Though the custom control software can be used to trigger FLIM measurements at distinct locations in the field of view, we generally acquire FLIM data at each pixel in the field of view by connecting a commercial galvanometer controller board and substituting the customized control software with commercial acquisition software (GVD-120, SPCM, Becker & Hickl GmbH).

The sample arm of the system's fiber-based spectral-domain OCT [18] hardware shares the imaging objective with the TPM and confocal instrumentation, but it utilizes separate scanning optics. Since optimal scanning protocols and beam geometry for OCT are, in general, significantly different than for TPM and/or confocal microscopy, our multimodal microscope design with two separate scanning arms allows optimal utilization of each imaging modality. OCT excitation is provided by a low-coherence, fiber-coupled superluminescent diode (λ: 856 ± 27 nm, Exalos, Inc. Langhorn, PA, USA). OCT galvanometer scanners (6210 H, Cambridge Technology, Inc) are relay imaged onto the back focal plane of the objective. The OCT scanning arm telescope can be adjusted (e.g. scan and tube lenses can be replaced) to enable applications requiring different lateral resolution. To achieve long A-scan range when using high-magnification objectives required for TPM, the OCT beam diameter must be reduced by a telescope before the objective to <1 mm. The SD-OCT spectrometer uses a 12- bit line scan camera (2048 pixels, 28 kHz line rate, AViiVA SM2 camera, e2v semiconductors, Chelmsford, Essex, UK). The typical incident power at the sample is ~1.5 mW, enabling a maximum detection sensitivity of 99 dB. Data acquisition is performed using a PC with a Horizon Link frame-grabber (i2S) and control is performed using an NI PCI 6731 data-acquisition card (National Instruments, Austin TX) and custom software written in LabView (National Instruments, Austin, TX).

LSCI of relative blood flow [19] is made possible using a CCD camera ($CoolSNAP_{fx}$, Roper Scientific) and custom-written software [20] in LabWindows CVI (National Instruments, Austin, TX). LSCI is performed using a 905 nm laser diode as a light source that can be directed into the OCT sample arm via a movable mirror. During LSCI, the OCT dichroic mirror is replaced with a polarizing beam splitter cube, which allows simultaneous LSCI and TPM imaging. Speckle signal is directed towards a CCD camera via another dichroic mirror (q880sp, Chroma Technology Corp) and subsequently filtered by a band pass detection filter placed in front of the camera. By removing the detection filter, the CCD is also useful for collecting reflectance images of the brain surface. For these measurements, a

#248448 Received 25 Aug 2015; revised 9 Nov 2015; accepted 14 Nov 2015; published 20 Nov 2015

broadband tungsten lamp (SpectraPhysics) coupled through an excitation filter ($\lambda = 570 \pm 5$ nm) and fiber bundle is used as the excitation source. Although results are not presented herein, incorporating a motorized filter wheel with multiple filters in front of the lamp or utilizing an array of LEDs with different colors easily enables multispectral optical intrinsic signal imaging (OISI) of relative changes in oxy- and de-oxy hemoglobin concentration and blood volume [21, 22].

Multiple PCs are required to operate the data acquisition control boards in the microscope. Confocal, TPM, and OCT imaging utilize custom-built software programs designed in LabView and C for controlling and synchronizing scanner mirrors, shutters, and detectors. The programs feature customized scanning protocols optimized for our experimental applications. For confocal or TPM imaging, the software permits adjustable temporal gating of the excitation beam, enabling the user to adjust the duration of the excitation pulse to saturate a desired focal volume of phosphor. Importantly, rather than simple raster scanning, the software also allows the selection of individual locations or rectangular and circular patterns of discrete measurement locations This flexibility in measurement locations is useful for improving the technique's temporal resolution, and it prevents unnecessary measurements from areas in the field of view where the contrast agent may not be present. This feature is particularly useful for experiments that focus purely on intravascular measurements. The software also features a block paradigm for repeatedly measuring transients synchronized with a functional stimulus [13–15, 17]. In the case of OCT imaging, quantitative microvascular flow measurements are performed over a volume of tissue by implementing a fast OCT raster scan protocol that collects 160 separate B-scans with 840 A scans per B-scan. A slower protocol is used to collect OCT-based angiograms, which collects 450 separate B-scans with 32760 A scans per B-scan [18]. To collect faster transient measurements of relative blood flow, single planar B-scans are rapidly collected with either 2800 or 4100 A-scans per B-scan [12]. Collecting phosphorescence lifetime data, both on its own or when coupled with another modality such as OCT for simultaneous multimodal measurements, requires synchronized coordination between 2 and 3 PCs. To maintain synchronicity, the custom control software on each machine features a combination of TCP/IP communication protocols for priming the data acquisition boards and delivering and receiving TTL trigger pulses to initiate simultaneous acquisition on each PC. For LSCI and OISI measurements, accurate timing can also be maintained by recording frame readout signal of the CCD.

2.2 Animal preparation

Our *in vivo* experiments of cerebral blood flow and energetics typically involve imaging through a sealed cranial window in anesthetized mice and rats. Depending on the type of study, imaging through a thinned skull and/or in awake animals can be also performed. In addition, animal preparation frequently involves a tracheotomy and mechanical ventilation, enabling precise control of inspired gas fractions, cannulation of the femoral artery and vein for both intravascular delivery of anesthesia and dyes and for monitoring systemic blood gases and pH. Physiological signals such as heart-rate, arterial blood pressure, expired pCO_2, and body temperature are monitored continuously during surgical preparation and the experiment [23]. Exogenous contrast agents for functional imaging of parameters, such as pO_2 or calcium dynamics, or morphological contrast, such as microvasculature or astrocytic cell bodies, are administered by either intravascular injection, microinjection into the cortical tissue, or topical application [13]. All animal procedures are performed in accordance with protocols approved by the Institutional Animal Care and Use Committee at Massachusetts General Hospital.

#248448 Received 25 Aug 2015; revised 9 Nov 2015; accepted 14 Nov 2015; published 20 Nov 2015

3. Results

3.1 Intravascular pO_2 and microvascular blood flow

Our multimodal imaging system has proven useful for monitoring several metrics of cerebral energy metabolism *in vivo*. Figures 2(a)-2(b) display representative confocal measurements of microvascular pO_2 and OCT observations of microvascular flow collected simultaneously from the rat cerebral cortex. Using confocal microscopy and OCT, precise, absolute measurements of these parameters were obtained simultaneously in individual microvessels over fields of view ranging from ~0.5-3 mm, enabling high-resolution observations of localized stimulus-induced activation of the somatosensory cortex along with neighboring, unperturbed cortical regions. An angiogram of the pial surface based on the phosphorescence intensity of the oxygen-sensing phosphorescent dye Oxyphor R2 [24] administered intravascularly is featured in Fig. 2(a). Pial arterioles and venules have been pseudo-colored red and blue, respectively. The angiogram, obtained from averaging two intensity measurements at each pixel, required ~13 seconds to scan over the full field of view. Specific intravascular locations were then selected to collect longer phosphorescence lifetime measurements of intravascular pO_2. Absolute pO_2 can be computed from the numerically-fitted phosphorescence lifetime using an experimentally-derived nonlinear Stern-Vollmer-like relationship, developed for greater accuracy of oxygen measurements [25]. The displayed pO_2 values at each location represent the average value of pO_2 measurements collected every 5 seconds over 2 minutes during baseline physiological conditions. Volumetric OCT measurements of the axial projection of red blood cell velocity were collected simultaneously, and the corresponding absolute cerebral blood flow measurements (μL/min) [18], representing the average value of measurements collected every 7 seconds for 2 minutes, are displayed beneath the pO_2 values. Although arterial oxygen and red blood cell velocity were always significantly higher than venous levels, both arterial and venous pO_2 demonstrated notable heterogeneity over short distances, illustrating that considerable heterogeneity in pO_2 and microvascular blood flow exists within a single resolvable voxel from fMRI or PET. pO_2 levels were also found to decrease as arterioles branched into smaller diameter arteriolar segments [14].

Measurements with higher temporal resolution can be performed by limiting the number of pO_2 measurement locations and collecting relative CBF from OCT B-scans rather than scanning a volume. Figure 2(b) displays example transient profiles of intravascular pO_2 and relative CBF from specific locations in an artery and vein, respectively, in response to a 4-second-long somatosensory electrical forepaw stimulus. The profiles represent the mean ± standard errors of pO_2 and rCBF averaged over 20 stimulus trials, during which 4-sec electrical pulse trains (0.3 ms pulse duration, 3 Hz) were delivered to the forepaw with 20 second interstimulus interval. In general, we observed in venules lower baseline levels and, consequently, more pronounced relative changes in both pO_2 and relative CBF compared to arterioles. In venules, a significant delay was observed between the increase in flow and the increase in oxygenation, indicative of the transit time and filling time through the underlying capillary network. Smaller diameter arterioles demonstrate a greater change in oxygen content than larger ones, further supporting the notion that oxygen extraction occurs in arteries. Although the relative change in pO_2 is smaller in arterioles compared to venules, the onset and peak time of oxygenation change occur significantly faster in arterioles. While the cerebral blood volume fraction is reportedly much less in the arterial compartment relative to the venous compartment [26], our observations indicate that the contribution from arterioles to the Blood Oxygenation Level Dependent (BOLD) signal observed with functional MRI, particularly the earlier part of the stimulus-induced response, may be more substantial than generally assumed [14].

#248448 Received 25 Aug 2015; revised 9 Nov 2015; accepted 14 Nov 2015; published 20 Nov 2015

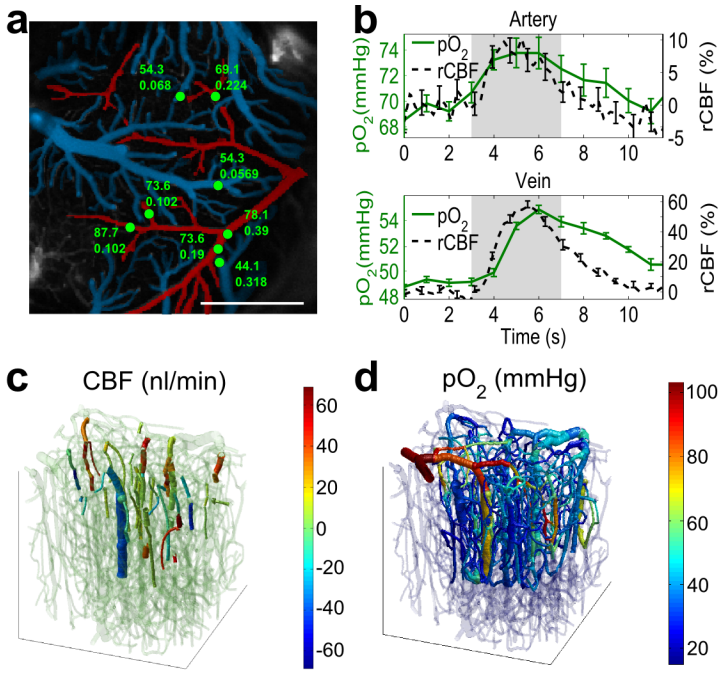

Fig. 2. Intravascular measurements of pO_2 and CBF (**a**) Color-coded, *in vivo* angiogram collected with confocal microscopy, green points represent locations at which pO_2 (mmHg) and absolute CBF (μL/min) were measured simultaneously with confocal microscopy and OCT, respectively. Scalebar: 1mm. (**b**) Representative traces of pO_2 and relative CBF collected during somatosensory stimulus (4-sec pulse train, 0.3 mS pulse duration, 3 Hz, administered to the forepaw during the shaded region) [14]. (c) and (d) Co-registration of the Two-Photon Microscopy and OCT data from the upper 650 um in a mouse somatosensory cortex. (c) The OCT measurements of blood flow. Measured blood flow values in penetrating arterioles and surfacing venules were color-coded and overlaid on the segmented microvascular structure. Positive CBF values correspond to upward flow in venules, while negative indicates downward flow in arterioles. The data were previously co-registered with the vascular stack in (d). (d) Segmented microvasculature with the intravascular pO_2 measurements obtained by TPM. Mean vascular segment pO_2 measurements were color-coded and overlaid on the segmented microvascular structure [15].

Two-photon microscopy imaging of pO_2 [27] can image much deeper into optically scattering cortical tissue [13] than confocal pO_2 imaging. Since both TPM imaging of pO_2 and OCT imaging of CBF allow measurements deep into the scattering brain tissue with high resolution, their combination presents a natural synergy that may become a critical tool to help us elucidate the mechanisms that secure sufficient oxygen delivery in microvascular domains during brain activation, and provide some metabolic reserve capacity in diseases that affect either microvascular networks or the regulation of cerebral blood flow (CBF) [15, 28]. Figures 2(c) and 2(d) show examples of segmented cortical vasculature overlaid with microvascular pO_2 and CBF measurements performed with TPM and OCT [15], respectively. In both panels, vascular morphology is displayed in gray and was obtained by computationally segmenting 3D vascular morphological stacks obtained by TPM imaging of blood plasma labeled by FITC-conjugated dextran. The segmentation of the microvasculature from the 3D FITC stacks obtained by TPM was performed by using a combination of the custom-written software for manual and semi-automatic graphing [29] and publicly available VIDA software [30]. pO_2 was measured in all types of microvessels (e.g. arterioles, capillaries, and venules) to a subsurface depth of ~450 μm using the oxygen-sensing nanoprobe PtP-C343 [27]. The co-registration of TPM and OCT data was performed by using custom-written software in Matlab (MathWorks, Inc.). We manually identified numerous

#248448 Received 25 Aug 2015; revised 9 Nov 2015; accepted 14 Nov 2015; published 20 Nov 2015

pairs of points in both 3D velocity projection map obtained by OCT and microvascular stack obtained by TPM, with each pair of points representing the same location in the microvasculature. The axial and lateral resolutions were ~5 & ~2 μm for TPM-based pO_2 measurements and ~6.4 & ~11 μm for OCT. However, the algorithms robustly accounted for these differences and accurately co-registered the volumetric data sets. Based on the selected pairs of points, the OCT velocity projection map and computed absolute flow in selected vascular segments were spatially transformed onto the TPM microvascular stack. Since the current OCT light source spectrum (λ: 856 ± 27 nm) overlaps with the 2-photon excitation of the pO_2-sensitive dye (840 nm), in these measurements pO_2 and CBF data were acquired sequentially with a few minutes gap between imaging. Despite the delay between measurements, the absence of pronounced metabolic perturbations, as determined by analysis of physiological parameters, provides assurance that the blood flow and oxygenation did not vary significantly between the TPM and OCT measurements. Replacing the OCT light source with one that features a higher central wavelength (e.g. 1300 nm) will allow true simultaneous two-photon and OCT measurements.

The presented multimodal measurements provide the framework for detailed investigations of cerebral oxygen delivery. Such information is critical for our understanding of not only normal brain physiology, but also the relation between progression of microvascular dysfunction and neurodegeneration in various brain diseases [31], and for attempts to develop a quantitative interpretation of existing and emerging brain imaging modalities [29–31].

3.2 Extravascular pO_2 and NADH autofluorescence

Measurements of microvascular blood flow and oxygenation are tremendously useful for evaluating brain function and physiology; however, observations of hemodynamic parameters reflect downstream effects of neuronal activity. Figure 3 displays metabolic measurements observed in the cortical tissue of rats and mice, providing a more direct indication of neuronal energy metabolism. Figures 3(a)-3(b) show high resolution measurements of pO_2 in cortical tissue in rats, obtained by pressure-injecting the nanoprobe PtP-C343 into cortical tissue before sealing the cranial window [13]. TPM imaging of cortical tissue pO_2 has the unique capability to provide minimally-invasive, extensive mapping of extravascular pO_2 space with high spatial and temporal resolution. Our results have shown that baseline tissue oxygenation and stimulus-induced changes are highly heterogeneous and vary considerably depending on proximity to vasculature [13, 32]. Figures 3(c)-3(d) display lifetime and intensity-based measurements of the intrinsic autofluorophore nicotinamide adenide dinucleotide (NADH), the ubiquitous electron carrier that performs critical roles in both anaerobic and aerobic metabolism. Lifetime analysis of the time-resolved fluorescence profile permits the resolution of multiple components with distinct fluorescence lifetimes. Reports suggest that these multiple components of NADH fluorescence represent different enzyme-bound formulations of NADH, and furthermore, the relative proportions of these components may reflect different steps of glycolysis and oxidative phosphorylation [33, 34]. Example recordings obtained

#248448 Received 25 Aug 2015; revised 9 Nov 2015; accepted 14 Nov 2015; published 20 Nov 2015

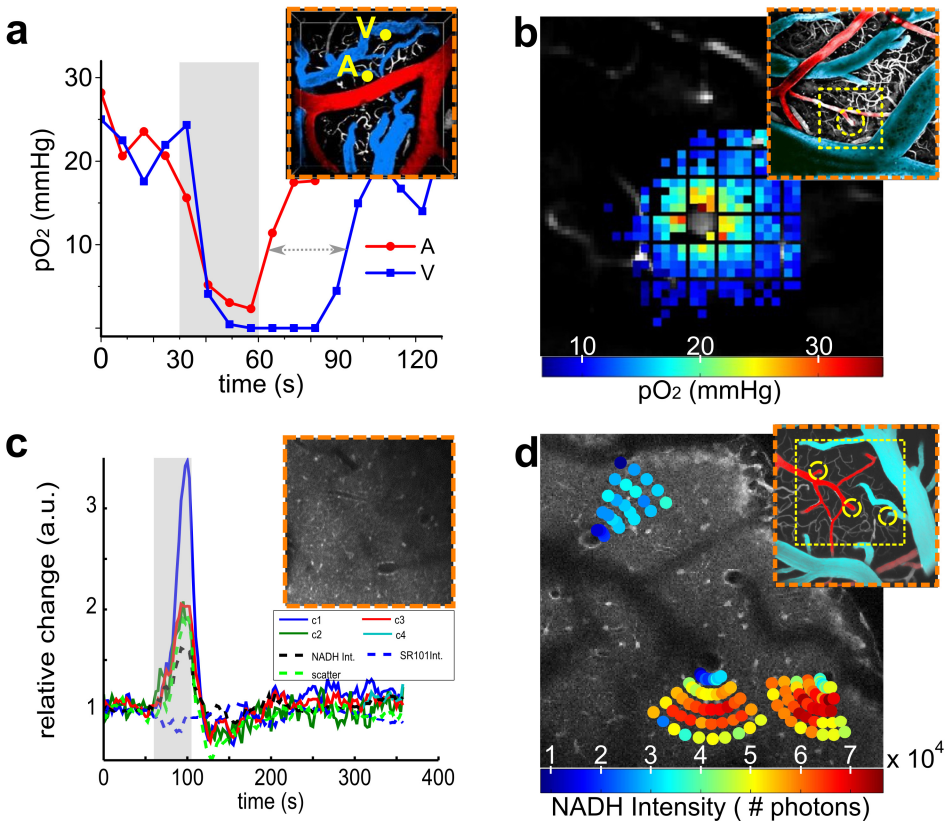

Fig. 3. TPM-based, extravascular measurements of pO_2 and NADH autofluorescence (**a**) pO_2 traces recorded near an arteriole (red) and venule (blue) during a brief period (30s) of anoxia [13] (**b**) spatial distribution of pO_2 in tissue surrounding a diving arteriole. (c) Representative traces of the normalized, amplitude-weighted lifetimes of distinct enzyme-bound formulations of NADH recorded with TPM FLIM during anoxic period (45s), averaged over the entire field of view [16] (**d**) spatial distribution of NADH intensity in tissue surrounding diving arterioles and a diving venule.

during transient metabolic perturbations can be seen in Figs. 3(a) and 3(c). In both plots, the shaded region corresponds to a brief anoxic period (30 or 45 s) induced by cessation of breathing (transient ventilator stop). Higher temporal resolution was achieved for these measurements by reducing the number of total measurement points, yielding measurement intervals of ~1s for pO_2 and 2.5 s for NADH. For each measurement, time-resolved phosphorescence or fluorescence measurements were recorded. pO_2 was computed by first fitting for the phosphorescence lifetime and calculated using the Stern-Vollmer relationship. NADH fluorescence was modeled as the sum of 4 exponential terms (c1-c4) and a small offset. As seen in Fig. 3(a), halted breathing leads to an immediate, drastic drop in extracellular pO_2 in the cortex. Conversely, as seen by the normalized, amplitude-weighted lifetimes of c1-c4 and the overall NADH intensity profiles in Fig. 3(c), reducing the available oxygen results in an increase in fluorescence amplitude of all NADH components, a consequence of diminished rates of oxidative phosphorylation compared to TCA cycle activity. The curves were obtained by interpolating over the 2.5 second-long measurement intervals. Characterization of this anoxia model in 10 different animals revealed a significant difference between some or all of the NADH components for kinetic features such as rise time and maximum change [16]. Restoration of breathing leads to an immediate drop in NADH levels and a more gradual return of pO_2 to baseline levels.

#248448 Received 25 Aug 2015; revised 9 Nov 2015; accepted 14 Nov 2015; published 20 Nov 2015

As shown in Figs. 3(b) and 3(d), our system can perform fluorescence and phosphorescence lifetime-based measurements of both pO_2 and NADH at discrete locations in the field of view. Separate excitation wavelengths (λ_{po2} = 840 nm, λ_{NADH} = 740 nm) and a spectral overlap in emission between NADH and coumarin fluorescence of Ptp-C343 currently prevents simultaneous measurement of these parameters, but novel probe developments are underway to enable this in the future. The ability to control the number and spatial patterns of measurement points is convenient not only for adjusting the temporal resolution; it also allows for straightforward analysis of the spatial variation of these metabolic parameters. Figure 3(b) and its corresponding inset show that tissue pO_2 values can vary by several tens of mmHg over distances as short as ~100 μm, illustrating the influence of proximity to oxygen-rich arterioles on the tissue pO_2 landscape.

Figure 3(d) displays multiple discrete locations at which FLIM measurements of NADH were collected in the rat cerebral cortex. The measurements were obtained by configuring our custom software to trigger single "Oscilloscope Mode" FLIM measurements in SPCM, the commercial TCSPC control software developed by Becker & Hickl GmbH [36]. The color of each point corresponds to the overall NADH intensity, calculated by integrating all photons in the TPSF at each location. The background image corresponds to the fluorescence intensity of Sulphorhodamine 101, administered topically to distinguish morphological features such as astrocytic cell bodies from blood vessels and neuropil. The fan geometry of measurement points provides a simple means to analyze spatial gradients from cylindrical sources and sinks such as ascending and descending cortical vessels. In select cases, a modest gradient can be observed in NADH intensity with proximity to blood vessels, with more distant regions having increased NADH intensity. pO_2 measurements demonstrate more robust gradients, with oxygen levels decreasing pronouncedly at increasing distances from arterioles.

3.3 Microvascular angiography, blood velocity, and NADH autofluorescence

While OCT enables absolute quantitation of microvascular blood flow in individual microvessels, the technique generally requires large amounts of computer memory and offline post-processing. OCT is still not well suited to display CBF images during an experiment with ~1 s temporal resolution and over a few millimeters field of view. However, this requirement is critical for numerous investigations. In our system, LSCI can easily be coupled with either TPM or confocal imaging and enables real-time assessment of relative cerebral blood flow (rCBF) and its pathology-related heterogeneity while also requiring less disk space and processing. For experiments involving localized metabolic perturbations, large field of view LSCI-based measurement of rCBF is critical to quickly identify metabolically-distinct cortical regions suitable for high magnification measurements, such as the boundaries of the ischemic core, penumbra, and non-ischemic tissue in focal ischemia. LSCI measurement is also important to monitor fast CBF transients associated with the neuronal functional activation, periinfarct depolarizations, or epileptic seizures, while simultaneously measuring cortical tissue structural and functional parameters with high resolution using TPM and/or OCT. Figure 4 displays reflectance-, LSCI- and TPM- based measurements of mouse cortical tissue after distal occlusion of the middle cerebral artery (MCA). The color-coded map of rCBF was measured with LSCI and overlaid on the gray-scaled reflectance image in Fig. 4(a). The grey area represents ischemic territory, identified as areas where rCBF was less than 25% of the maximum observed value, while colored regions represent cortical tissue regions that remained perfused. The dashed yellow square identifies the field of view for TPM-based measurements of the cranial window displayed in Figs. 4(b) and 4(c). The smaller, dashed boxes illustrate tissue regions measured with higher resolution using the 20x objective. Although vessels can be seen in the lower portion of the reflectance image in Fig. 4(a), including a branch of the MCA extending upward from the lower right hand corner (solid white arrow, Fig. 4(a)), these vessels are not observable in Fig. 4(b), which depicts the

#248448 Received 25 Aug 2015; revised 9 Nov 2015; accepted 14 Nov 2015; published 20 Nov 2015

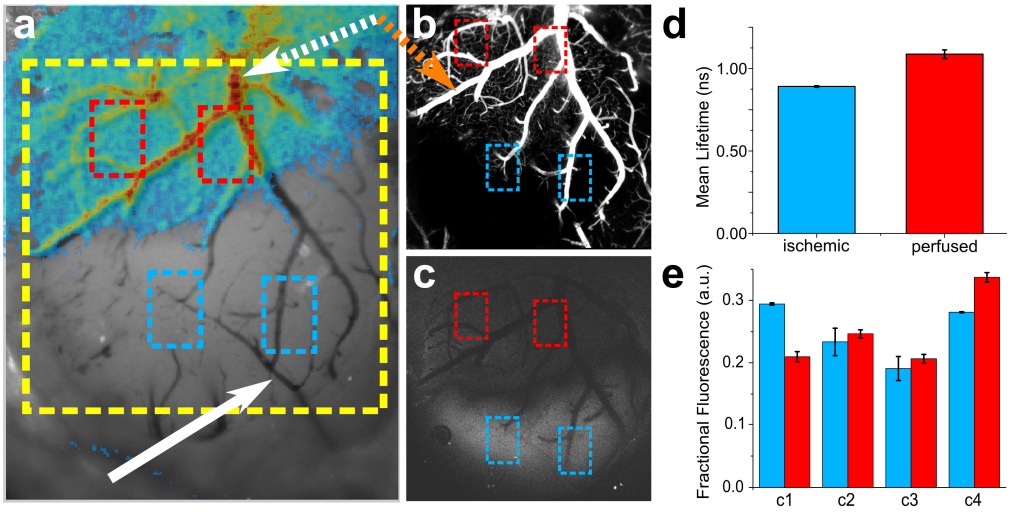

Fig. 4. Spatial variability of relative cerebral blood flow (rCBF) and energy metabolism during focal ischemia (a) 580 nm reflectance image of the cranial window after distal occlusion of the middle cerebral artery, overlaid with color-coded relative cerebral blood flow measured with LSCI. Colored regions depict areas where rCBF stayed above 25% of the maximum rCBF value after occlusion. Dashed yellow rectangle represents the large field of view for 2-photon imaging over the entire cranial window (figs b and c). Dashed rectangles indicate areas imaged with higher magnification TPM FLIM of NADH, with red depicting well-perfused regions and blue indicating ischemic territory. Solid arrow identifies occluded MCA branch; dashed arrow indicates draining venule along the pial surface (b) Maximum intensity projection of intravascular FITC fluorescence, measured with TPM microscopy. (c) Corresponding NADH intensity fluorescence of the brain tissue, (d) mean lifetime values of intrinsic NADH, measured with TPM FLIM, in ischemic regions and perfused regions (e) Fractional fluorescence of the 4 "components" of NADH (c1 – c4 depict component 1 – component 4), observable by TPM-FLIM.

maximum intensity projection of a depth-resolved stack of TPM images measuring intravascular, dextran-bound FITC over a ~600 µm range of depth. The FITC was administered by intravenous injection approximately 3 hours after the occlusion. In the perfused regions, a large pial venule on the cortical surface can be resolved (dashed white arrow, Fig. 4(a); dashed orange arrow Fig. 4(b)) along with several smaller capillaries located 100s of µm below the surface, while the ischemic area demonstrates no evidence of blood flow and appears black. As seen in Fig. 4(c), the corresponding NADH fluorescence intensity appears substantially brighter in the ischemic territory. The increased relative brightness of NADH is suggestive of a critical deficit in oxygen supply and impaired mitochondrial function that is spatially heterogeneous throughout the cortex; however, quantitative interpretation of NADH intensity is confounded by factors such as optical scattering, hemoglobin absorption, and the multiple roles played by NADH in glycolysis and oxidative metabolism. FLIM-based measurements of NADH were collected in the ischemic and perfused regions to more quantitatively evaluate variations in metabolic activity. Lifetime-based measurements of fluorescence are insensitive to factors affecting intensity and show potential for resolving shifts in aerobic and glycolytic activity [34, 36]. As seen in Fig. 4(d), our 4-component based analysis [16] revealed that ischemic brain tissue displays a significantly different mean lifetime than well perfused tissue. Figure 4(e) displays the differences between ischemic and perfused tissue in the fractional fluorescence of components 1-4, which represents the relative contribution of each component to the total fluorescence [34]. The reduced mean lifetime and increased fractional fluorescence of component 1 are consistent with other reports, which suggest that a bottleneck in the electron transport chain, induced by either inhibiting complex IV or reducing oxygen supply, yields a

#248448 Received 25 Aug 2015; revised 9 Nov 2015; accepted 14 Nov 2015; published 20 Nov 2015

relative increase in the shortest-lifetime component of NADH, reflecting a greater presence of unbound, 'free' NADH [16, 34, 35, 37, 38]. These observations set the stage for detailed studies investigating stroke, reperfusion injury, and prospective therapeutic techniques.

4. Conclusion

We presented a customized microscope that couples the benefits of multiple optical imaging techniques into a single platform. The advantage of combining two-photon microscopy with OCT for structural and functional studies was recognized previously, and various multi-modal systems based on these two technologies have been demonstrated [39–41]. Similar to another recently-reported system [42, 43], our multimodal microscope utilizes two separate optical scanning paths for laser scanning microscopy (two-photon or confocal) and OCT, enabling greater flexibility of scanning protocols when coupling these modalities. The system also features additional tools (OISI and LSCI), all specifically tuned to enable multifaceted characterization of cerebral energetics and its pathological alterations in small animals. Although our system provides multiple imaging capabilities, both 2-photon microscopy and OCT show particular promise for enabling minimally-invasive characterization of cerebral blood flow, microvascular architecture, and oxygen delivery in the living brain with unprecedented spatial resolution. Additional techniques such as confocal microscopy and LSCI enable measurement of oxygenation and blood flow over larger fields of view with more economical hardware and resources, as well as less intensive data processing. Such capabilities make these imaging modalities well-suited for investigations that require the rapid assessment of heterogeneous CBF distribution or oxygenation over large fields of view, such as focal ischemia studies requiring real time evaluation of ischemic territory and penumbra. Additionally, rapid monitoring of CBF and pO_2 over the large field of view is important in the presence of sporadic physiological events such as periinfarct depolarizations or seizures. 2-photon and confocal microscopy afford the additional ability to assess alterations in cellular signaling, metabolic activity, and morphology with high spatial and temporal resolution *in vivo*. The application of all of these combined tools will prove helpful for identifying mechanisms that ensure adequate oxygen delivery in microvascular domains in a healthy brain, and provide some insight into the etiologies of debilitating diseases that adversely affect critical metabolic parameters, such as the organization microvascular networks, the regulation of cerebral blood flow (CBF), or mitochondrial function in neurons, glia, and vascular endothelial cells.

In the future, replacing the OCT setup with one based on a light source centered around 1300 nm, integration of electrophysiological measurements such as patch clamp electrodes or EEG, and development of better pO_2-sensitive probes will further enhance the capabilities of the system to assess critical parameters of cerebral physiology.

Acknowledgments

This work is supported by the National Institutes of Health (NIH) (K99AG042026, R00NS067050, P50-NS010828, R01-NS057476, R01-EB000790, R24NS092986, R01NS091230, R01EB018464) and the American Heart Association (AHA) (11SDG7600037). The authors wish to thank Drs. Anna Devor and Louis Gagnon for their help with data acquisition, processing, and interpretation. We also thank Svetlana Ruvinskaya, Dr. Weicheng Wu, and Dr. Buyin Fu for their extensive efforts with animal preparation, and we extend our deepest thanks to Drs. Cenk Ayata and Fumiaki Oka for their guidance with the dMCAO model.

#248448 Received 25 Aug 2015; revised 9 Nov 2015; accepted 14 Nov 2015; published 20 Nov 2015